Phase diagram of the spin-$\frac{1}{2}$ triangular J_1-J_2 Heisenberg model on a three-leg cylinder

S. N. Saadatmand,[1,*] B. J. Powell,[2] and I. P. McCulloch[1]

[1]*ARC Centre for Engineered Quantum Systems, School of Mathematics and Physics, The University of Queensland, Saint Lucia, Queensland 4072, Australia*

[2]*School of Mathematics and Physics, The University of Queensland, Saint Lucia, Queensland 4072, Australia*

(Received 25 March 2015; revised manuscript received 30 April 2015; published 9 June 2015)

We study the phase diagram of the frustrated Heisenberg model on the triangular lattice with nearest- and next-nearest-neighbor spin-exchange coupling, on three-leg ladders. Using the density-matrix renormalization-group method, we obtain the complete phase diagram of the model, which includes quasi-long-range 120° and columnar order, and a Majumdar-Ghosh phase with short-ranged correlations. All these phases are nonchiral and planar. We also identify the nature of phase transitions.

DOI: 10.1103/PhysRevB.91.245119 PACS number(s): 75.10.Jm, 75.10.Pq, 75.10.Kt, 75.40.Mg

I. INTRODUCTION

Quantum magnetism in reduced dimensions gives rise to a fascinating range of behaviors [1–3]. In one-dimensional (1D) systems, powerful analytical and numerical methods have allowed a deep understanding of phenomena such as fractionalization [4], dimerization [5], and symmetry protected topological order [6,7]. In two-dimensional (2D) systems, there remain many more open problems such as understanding spin liquids [8,9], intrinsic topological order [10,11], and the connection between exotic magnetic phases and unconventional superconductivity [9,12]. Few-leg ladders are a vital intermediate class as they allow for the application of accurate numerical methods [13] available for large 1D systems, while also providing important insights into new physics occurring in the crossover to two dimensions [14,15].

In an unfrustrated system, such as the nearest-neighbor (NN) Heisenberg model on the square lattice, all of the terms in the Hamiltonian can be minimized simultaneously. This tends to favor long-range order in two dimensions. Therefore, frustrated systems are excellent candidates in which to search for exotic phases of matter without conventional ordering [8,9].

The spin-$\frac{1}{2}$ triangular Heisenberg model (THM) is a prototypical model for frustrated magnets in two dimensions [2]. In 1973, Anderson [16] suggested that the resonating-valence-bond (RVB) state could play a pivotal role in the description of novel magnetic materials, and his conjecture that the ground state of the spin-$\frac{1}{2}$ THM would be an RVB state provoked much interest. However, studies of this model have failed to find an RVB state and the evidence [17,18] is now very strong that for the pure isotropic model with nearest-neighbor interactions the ground state is a 120° magnetically ordered state [1]. Variants of the THM describe some properties of organic materials [8,9] such as κ-(BEDT-TTF)$_2$Cu$_2$(CN)$_3$, EtMe$_3$Sb[Pd(dmit)$_2$]$_2$, EtMe$_3$P[Pd(dmit)$_2$]$_2$, and Mo$_3$S$_7$(dmit)$_3$ [20,21] and also some quasi-two-dimensional inorganic materials [8,9,22–25] such as RbFe(MoO$_4$)$_2$, Ba$_3$CoSb$_2$O$_9$, Cs$_2$CuBr$_4$, and Cs$_2$CuCl$_4$.

In one dimension the prototypical frustrated system is the zig-zag chain, which has an exact solution at the Majumdar-Ghosh point [3,5] where the NN coupling is twice the next-nearest-neighbor (NNN) coupling. The ground state is characterized by long-range dimer order and is twofold degenerate. As we show below, an NNN Majumdar-Ghosh phase is stabilized in a large region of the phase diagram of the three-leg triangular ladder.

So far the THM has been mostly considered with only NN exchange coupling, but additional interactions or anisotropies may stabilize exotic states. A natural choice for an additional interaction, while retaining isotropy, is an NNN coupling to add further frustration effects. In this paper we study the J_1-J_2 THM on a width 3 cylinder as a simplified version of the full 2D model, but readily accessible to numerical methods. The ladder model has clear connections to the 2D THM and also extrapolates smoothly to the Majumdar-Ghosh point of the zig-zag chain. The J_1-J_2 THM in two dimensions has been previously studied using semiclassical spin-wave theories (SWTs) and exact diagonalization (ED) [18,19,26–29], but these studies did not cover the physics of the whole phase diagram. Recently, a coupled cluster method (CCM) study [30] and quantum Monte Carlo (QMC) studies [31,32] have identified a phase in this model that is a candidate for a spin liquid. Magnetically ordered states in a variety of classical $O(3)$ models with J_1-J_2-J_3 interactions have been studied by Messio, Lhuillier, and Misguich [33], finding several different "regular magnetic orders" relevant to the triangular lattice, including planar and nonplanar 120° states.

The lattice we consider is shown in Fig. 1. The Hamiltonian is

$$H = J_1 \sum_{\langle i,j \rangle} \mathbf{S}_i.\mathbf{S}_j + J_2 \sum_{\langle\langle i,j \rangle\rangle} \mathbf{S}_i.\mathbf{S}_j, \tag{1}$$

where $\langle i,j \rangle$ ($\langle\langle i,j \rangle\rangle$) indicates that the sum is over all NN (NNN) couplings. To cover the full range of couplings, we introduce the following parametrization:

$$J_1 = J\cos\theta, J_2 = J\sin\theta, \tag{2}$$

where the J is the unit of energy and henceforth we fix $J = 1$. The main difficulty in studying the lattice shown in Fig. 1 is frustration. The lowest-energy state of the antiferromagnetic (AFM) Heisenberg model on a square lattice has Néel order [2]. This cannot be formed on an equilateral triangular lattice, and as a result there is competition between terms in the Hamiltonian, Eq. (1), and they cannot simultaneously minimize their local energy. Therefore it is clear that the

*s.saadatmand@uq.edu.au

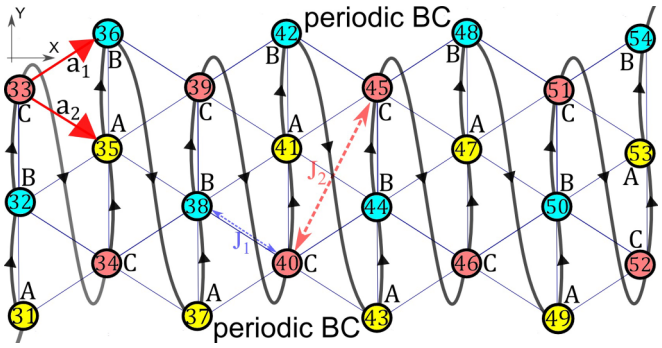

FIG. 1. (Color online) Lattice structure and mapping of the three-leg cylinder to the one-dimensional chain employed by the finite DMRG calculations. Spins sit on vertices. The lattice is tripartite and the sublattices are labeled A, B, and C. $\mathbf{a_1}$ and $\mathbf{a_2}$ are lattice vectors.

lowest-energy state must be a compromise, such as the 120° state. The 120° state on the triangular lattice is less stable than the Néel state on the square lattice [9,18], as the sublattice magnetization of the triangular lattice is significantly reduced compared to its classical value. Because of this reduced stability inherent to the triangular lattice, upon perturbing the Hamiltonian one may expect to see a variety of new phases.

There have been several numerical studies of the THM in the past. Exact diagonalization methods [18,26–28,34] suffer from the exponentially growing size of the Hilbert space, which is especially a problem in two or more dimensions, while QMC techniques [35] suffer from the sign problem for frustrated lattices, and projected entangled pair states (PEPSs) [36,37] for this model are complex and computationally costly, even though, in principle, PEPSs have good computational scaling properties in two dimensions. More recently some numerical methods have been developed that are especially useful for frustrated systems and applied to the THM, for example, the large-scale parallel tempering Monte Carlo [38] and some tensor networks methods including entangled-plaquette states [39] and the multiscale entanglement renormalization ansatz (MERA) [40].

On the other hand, matrix product states (MPSs) [41] have been around in various guises for a long time and are a good representation of the ground state of 1D chains and few-leg ladders. MPSs exploit the locality of the interactions for 1D ladders and compute a truncated Hilbert space that is well suited for describing ground states, as it satisfies the *area law* for the bipartite entanglement (see [36], and references therein). In particular, the density-matrix renormalization-group [41–43] (DMRG) method for finding the variational ground state is mature and highly efficient. A recent study [44] of different numerical methods suggested that the two-dimensional DMRG could be "one of the most powerful methods" for studying quantum lattice systems.

A study using the same method as this paper derived the phase diagram of the J_1-J_2 Heisenberg model on a kagome lattice, which also contains a rich variety of phases [45], including a spin liquid and magnetically ordered states. The THM on a three-leg ladder has been previously studied for anisotropic NN interactions with a magnetic field [46], and a phase diagram has been obtained. At the isotropic point, corresponding to $\theta = 0$ in our notation, it was shown that the introduction of a magnetic field, $-h\sum_i S_i^z$, causes the 120° state to evolve into commensurate planar phases with Y- and V-shape spin ordering on either side of a 1/3 magnetization plateau [46].

II. METHODS: MPS AND DMRG

In this paper we employ the MPS ansatz, keeping up to $m = 1000$ basis states, using the DMRG method for obtaining the ground-state wave function. The Hamiltonian has $SU(2)$ symmetry:

$$[H,\mathbf{S}] = 0. \tag{3}$$

Exploiting this symmetry in the calculations gives a significant improvement in efficiency, by reducing the dimension of the computational Hilbert space. Using $m = 1000$ $SU(2)$-symmetric basis states is equivalent to $m \approx 3000$ states with no [or just Abelian $U(1)$] symmetry. We performed both finite DMRG and infinite DMRG [47] (iDMRG) calculations. The latter exploits translational symmetry available in the thermodynamic limit.

Because MPS is fundamentally a 1D ansatz, to apply it to 2D models a mapping is necessary. We map the 1D chain of spins into a size $N = L \times 3$ chain in the YC configuration as shown in Fig. 1, where L is the length of the three-leg cylinder. The computational cost will scale approximately linearly with length, but still exponential with width, which is a limitation of this method. The model is on a cylinder, i.e., we use open boundary conditions (OBCs) in the long (horizontal) direction and periodic boundary conditions (PBCs) in the short (vertical) direction, so that the total number of NN or NNN bonds in the lattice is $3N - 12$. From finite size scalings of the energy and other order parameters, we found that sizes up to 30×3 are large enough to scale finite results properly into the thermodynamic limit.

In the case of iDMRG, one can classify all possible wrappings of the triangular lattice on an infinite three-leg cylinder, using a standard notation developed for single-wall carbon nanotubes [48]. We use the wrapping vector $\mathbf{C}_0 = (-3,3)$ in this notation. The unit vectors, $\mathbf{a_1}$ and $\mathbf{a_2}$, used to specify $\mathbf{C}_0$, are shown in Fig. 1. $\mathbf{C}_0$ preserves the tripartite symmetry on the infinite lattice. The pitch angle of this wrapping method is $\phi_0 = 90°$. The matrix product operator [43] (MPO) representation of the Hamiltonian has a three-site unit-cell in the direction of $\mathbf{C}_0$. One can show that $\mathbf{C}_0$ is the shortest possible wrapping vector that preserves tripartite symmetry. The minimum unit cell of the wave function, however, is 18 sites, as the smallest even size that preserves tripartite symmetry.

Error analysis

We use the variance to calculate systematic errors in the DMRG results. E.g., in the case of energy, we have $\sigma_E^2 = \langle\psi_v|(H-E)^2|\psi_v\rangle$. For energy errors, one needs to plot energy versus variance step by step for different numbers of states, m. The behavior of E versus σ_E^2 is expected to be linear. Any significant deviation from this linearity indicates that the DMRG calculation has not converged, possibly due to an insufficient number of basis states. An example of this

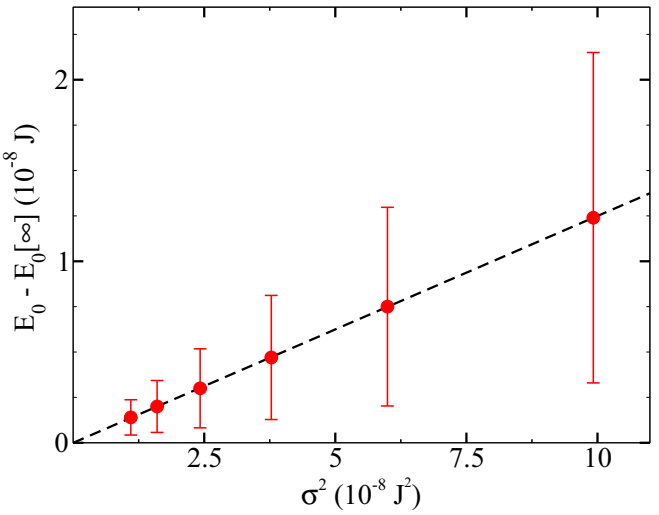

FIG. 2. (Color online) Energy vs variance for a 30×3 cylinder with $\theta = 25^\circ$. The linear extrapolation gives a good approximation for the exact ground-state energy.

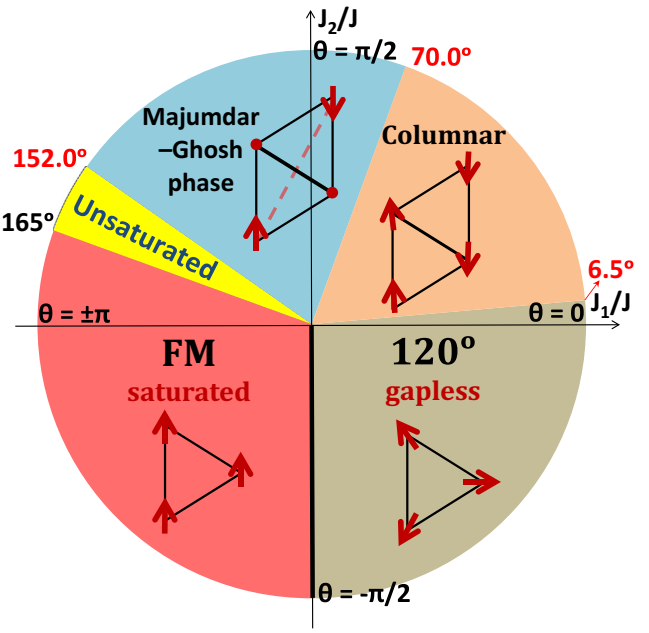

FIG. 3. (Color online) The calculated phase diagram of the J_1-J_2 THM on a three-leg cylinder. The phase transitions are indicated to a resolution of 0.5°. All transitions are second order except for $\theta = -\pi/2$, which is first order (marked by a thick black line).

calculation is shown in Fig. 2, for a 30×3 lattice with $\theta = 25^\circ$, for m between 500 and 1000. The ground-state energy extrapolated to the $m \to \infty$ limit is $E_0[\infty] = -46.94877331266(2)$. This method is similar to, but more robust than, the energy versus truncation error scaling that is typically used in DMRG calculations [43].

Throughout this paper the results are all converged with relative errors $\sim 10^{-12} - 10^{-8}$. Errors are smaller than symbol size for all plots except for the finite-size extrapolation of the spin gap in Fig. 15(a), where we show explicit error bars.

III. PHASE DIAGRAM

The calculated phase diagram of the J_1-J_2 THM is shown in Fig. 3. The dominant short-range ordering is sketched in the form of triangular or rhombic plaquettes. The model contains four well-defined phases. The different phases were determined by studying the ground-state energy (Sec. III B), spin–spin-correlation functions (Sec. IV), the chirality (Sec. V), 120° order parameter (Sec. VI), spin gap, dimer order parameter, and Binder cumulant (Sec. VII).

In order to better visualize the nature of the short-range correlations in each phase, Fig. 4 shows the NN and NNN bonds, colored according to the value and sign of the spin-spin correlation. The four phases are as follows.

(1) A **120**° state [cf. Fig. 4(a)] that exists in the fourth quadrant of Fig. 3 is critical (see Sec. VII below), with power-law correlations and gapless excitations. This is in contrast to the 2D model, which has long-range tripartite magnetic ordering. However long-range magnetic ordering is forbidden in our three-leg cylinder due to the Mermin-Wagner theorem [49], which excludes SU(2) symmetry-broken long-range order in one dimension. The 120° state is parity symmetric (P symmetric), time-reversal symmetric (T symmetric), and planar (see Sec. V below). We find that the NN spin–spin-correlation functions are C_6 symmetric in this phase (cf. Fig. 7); however, chiral correlators are C_3 symmetric, reflecting the "antiferrochiral" ordering (cf. Sec. V). This state persists in the first quadrant up to a quantum critical point at nontrivial $\theta_c \simeq 6.5^\circ$. The existence of the 120° state is consistent with spin-wave results of Jolicouer *et al.* [18], although the transition point of spin-wave calculations is located at $\theta_{\rm SWT} = \tan^{-1}\frac{1}{8} \simeq 7.125^\circ$ compared to our value of 6.5°.

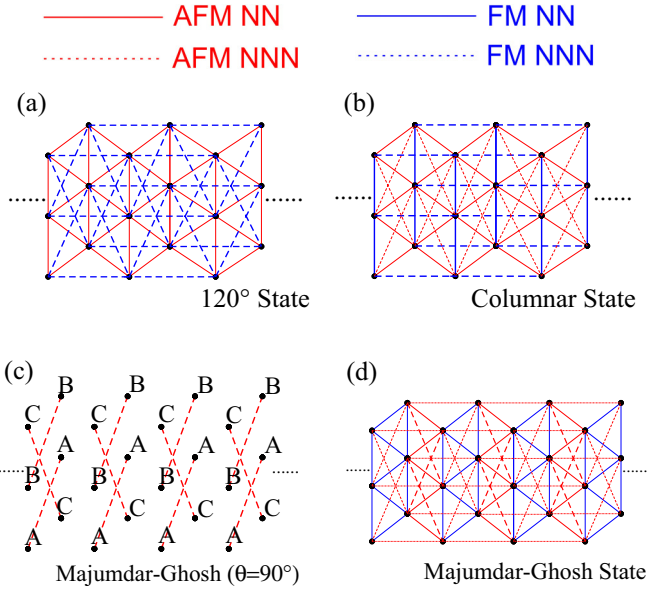

FIG. 4. (Color online) Visualizations representative of different phases of the THM on a cylinder. Thicker lines represent stronger bonds with red indicating antiferromagnetic bonds and blue indicating ferromagnetic.

(2) Upon increasing $\theta > 6.5°$, the system changes phase to a two-sublattice commensurate spin state with a columnar structure [cf. Fig. 4(b)], which is also gapless. This is consistent with the 2D model, which has long-range columnar order [30–32]. However, this ordering is forbidden in one dimension for the same reason as the 120° state. The columnar state is quasi-long-range, C_6 rotational symmetry broken, P symmetric, T symmetric, and planar. This phase can be thought of as a planar version of the standard G-type antiferromagnetism [50].

(3) At $\theta \simeq 70.0°$, there is a phase transition to a NNN Majumdar-Ghosh state. In this phase the system forms strong AFM bonds (dimers) along NNN bonds. Because of the finite width of the ladder and the periodic boundary conditions in the short direction, each site is NNN to some other site twice; e.g., the exchange interaction between sites 38 and 42 is twice that between site 38 and 44 (cf. Fig. 1). At $\theta = \pi/2$, the model is composed of three uncoupled sublattices in the form of two-leg spin ladders. The double counting of the NNN bonds means that the Majumdar-Ghosh Hamiltonian is realized in each sublattice, leading to three copies of the twofold degenerate Majumdar-Ghosh state with long-range dimer order, shown in Fig. 4(c). The Majumdar-Ghosh state is robust to small perturbations when one turns on the J_1 interactions, and evolves into the general form shown in Fig. 4(d), with weak NN bonds, either antiferromagnetic or ferromagnetic corresponding to the sign of J_1. We find, numerically, that this state persists throughout a large region in the first and second quadrants of Fig. 3. The Majumdar-Ghosh state has short-ranged correlations (cf. Fig. 9), and is C_6 rotational symmetry broken, translational symmetry broken, P symmetric, T symmetric, and planar.

(4) Upon further increasing of θ, the system undergoes a second-order phase transition at $\theta_c = 152.0°$ (see Sec. VII below). In a narrow region, $152° < \theta < 165°$ of Fig. 3, the ground state is a partially polarized ferromagnet that saturates to complete ferromagnetism for $\theta > 165°$.

A. Limiting cases

In our parametrization of the Hamiltonian, $\theta = 0$ is equivalent to $J_2 = 0$, and is simply the nearest-neighbor model. The ground state is the 120° state, in agreement with the semiclassical approach [18], with wave vector $\mathbf{Q} = (2\pi/\sqrt{3}, 2\pi/3)$ in our notation.

For $\theta = 90°$ ($J_1 = 0$), the model has only NNN interactions. This state is composed of three uncoupled spin ladders, one in each tripartite sublattice, forming a perfect Majumdar-Ghosh state of alternating singlet dimers [3,5]. The formation of this phase is a direct consequence of the three-leg form of the lattice, Fig. 1, which is wrapped around a cylinder resulting in three independent zig-zag spin chains with NN coupling J_2, and the double-counted bonds around the periodic boundary give an NNN coupling of $2J_2$. Thus, this state appears because of the restricted geometry of the three-leg ladder. On the other hand, in the 2D limit the Hamiltonian is instead three copies of the $\theta = 0$ model, hence the ground state will contain three copies of the 120° state, one on each sublattice, and a small J_1 will couple the otherwise independent sublattices. Thus the small-J_1 behavior for few-leg ladders is rather different to the bulk 2D behavior.

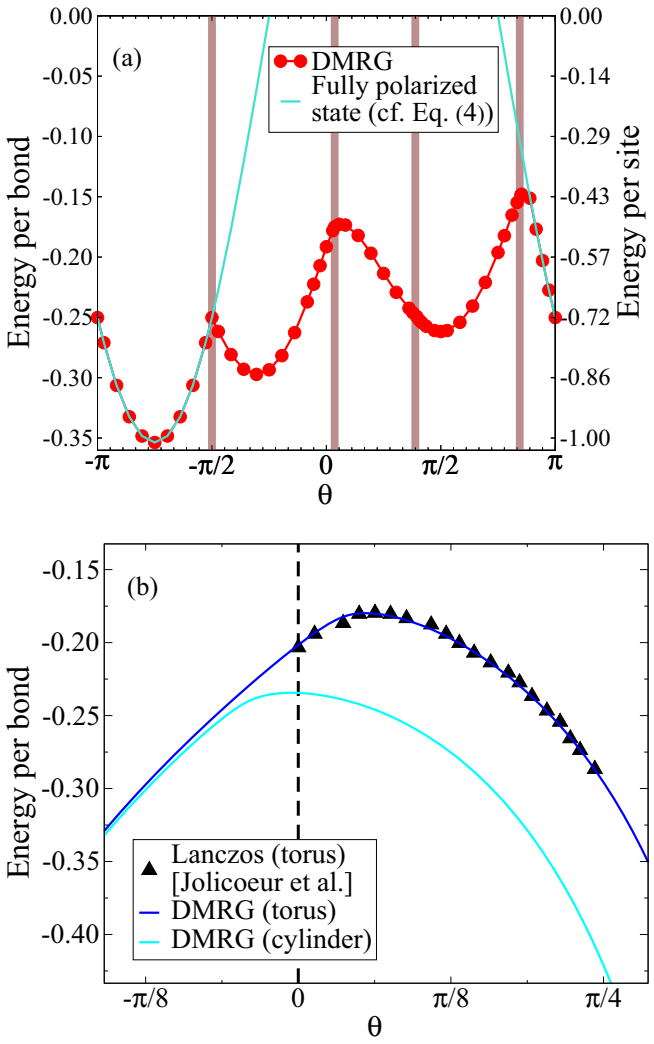

FIG. 5. (Color online) (a) Ground-state energy of the THM on a 30×3 cylinder. The transition at $\theta = -\pi/2$ is sharp and consistent with a first-order phase transition (cf. Sec. VII). The transition near $\theta \approx 160°$ suggests a second-order phase transition (cf. Sec. VII). Brown stripes indicate phase transitions. (b) Comparison of the energies of Lanczos and DMRG for the THM on a 4×3 lattice. Lanczos results are from Jolicoeur *et al.* [18]. DMRG and Lanczos show excellent agreement, but the boundary conditions clearly have a significant effect on the energy of this small lattice.

For $0 < \theta < \tan^{-1}(\frac{1}{8})$ the 2D model at the classical level ($S \to \infty$) has a 120° ground state [29] and for $\theta > \tan^{-1}(\frac{1}{8})$ it has a four-sublattice AFM Néel phase with an infinite manifold of degenerate ground states, selected by the "order from disorder" mechanism. Quantum fluctuations break this degeneracy, and the quantum model has a two-sublattice columnar (collinear) Néel state [30–32]. It is worth mentioning that the selection of the collinear order from the four-sublattice classical order can be understood analytically using group-symmetry analysis [51].

It is straightforward to show that for the classical J_1-J_2 THM, if one enforces the tripartite symmetry everywhere using a repeated three-site unit cell, the ground-state phase is simply

TABLE I. Comparison of the ground-state energies from different methods for the THM at $\theta = 0$.

Method	Cluster size	Boundary conditions	Energy per bond, $\varepsilon_0^{\theta=0}$
DMRG (this work)	4×3	Torus	$\leqslant -0.20164623520324(1)$
DMRG (this work)	60×3	Cylinder	$\leqslant -0.19053054(3)$
DMRG (this work)	Extrapolated to thermodynamic limit ($L \times 3$ lattices with $L \leqslant 60$)	Cylinders	$-0.189(2)$
iDMRG (this work)	Infinite	Three-leg cylinder	$\leqslant -0.189715084187(2)$
Schwinger boson [52]	$N = 12$	Torus	-0.1899
Ising expansion [53]	Theoretically thermodynamic limit		-0.187
Entangled plaquette states [39]	Extrapolated to thermodynamic limit (Clusters up to size $N = 324$)	Torus	$-0.18473(4)$
Coupled cluster method [30]	Extrapolated to thermodynamic limit		$-0.1840(1)$
Numerical diagonalization [54]	Extrapolated to thermodynamic limit (Clusters up to size $N = 27$)	Torus	-0.183 ± 0.003
QMC [34]	Extrapolated to thermodynamic limit		$-0.182(3)$
SWT [55]	Theoretically thermodynamic limit		-0.182
MERA [40]	Extrapolated to thermodynamic limit (Clusters up to size $N = 114$)	Torus	-0.18029

ferromagnetic (FM) for $J_1 < 0$ and the 120° state for $J_1 > 0$, independent of J_2.

B. Ground-state energy

In this section, we benchmark our results for the ground-state energy per nearest-neighbor (J_1) bond, ε_0. This is shown in Fig. 5. The energy per NN bond in the fully polarized ferromagnet is

$$\varepsilon_{\mathrm{FM}} = \tfrac{1}{4}(\sin\theta + \cos\theta), \tag{4}$$

which is shown in turquoise in Fig. 5(a).

There is a sharp transition appearing at $\theta = -\pi/2$, coinciding with the change from the FM to 120° state. The cusp suggests a first-order phase transition, which is confirmed by the local magnetization and order parameters. This is the only first-order transition that we find in the model, and is indicated by the thick black line in Fig. 3. On the right-hand side of Fig. 5(a), at $\theta_c \simeq 152.0°$, the derivative is continuous indicating that the transition from the Majumdar-Ghosh state to the FM is second order, which we verified by calculating the magnetization (see Sec. VII below).

Figure 5(b) is a comparison of DMRG energies with Lanczos results of Jolicoeur *et al.* [18]. They simulated the same model on a 12-site lattice with PBC in both directions, which is equivalent to a 4×3 torus in our representation. The choice of wrapping vector around the torus has little effect as long as the lattice translational and tripartite symmetries are preserved. Our DMRG results are in very good agreement with these Lanczos results.

Table I is a comparison between our DMRG energy and results from previous calculations for $\theta = 0$, i.e., the NN model in the 120° phase. For this point we performed a larger size calculation on a 60×3 cylinder, as there is no NNN frustration and the DMRG is easier to converge. The results in Table I suggest that the THM on a cylinder is a good approximation for the full 2D model.

C. Local magnetization

The squared magnetization per plaquette M^2_{ave} is presented in Fig. 6. This is calculated from the square of the local magnetization on a single plaquette:

$$M^2_{\mathrm{ave}} = \frac{1}{N_p} \sum_{\{A,B,C\}} (\mathbf{S}_A + \mathbf{S}_B + \mathbf{S}_C)^2, \tag{5}$$

where the sum is over all N_P plaquettes with vertices A, B, and C from their respective sublattice. The turquoise lines in Fig. 6 indicate the region where we find a partially polarized ferromagnetic ground state. The rapid but smooth change in local magnetization in this region is consistent with a second-order phase transition.

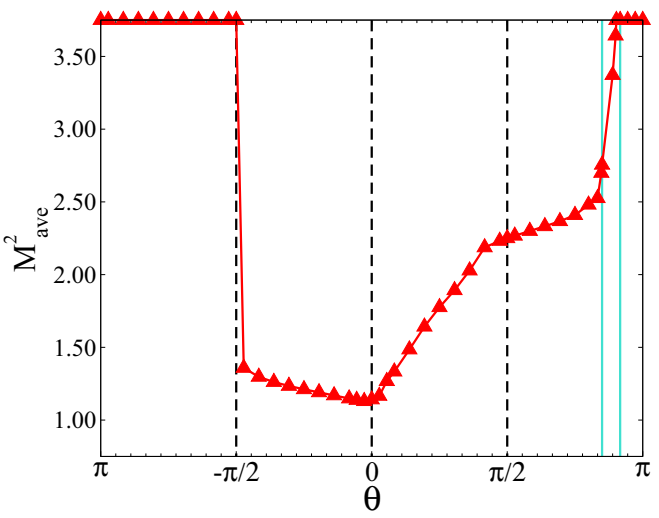

FIG. 6. (Color online) Average of squared magnetization per plaquette, Eq. (5), on a 30×3 cylinder. The vertical turquoise lines denote the partially polarized region at the second-order transition into the ferromagnetic state.

IV. SPIN-SPIN CORRELATIONS

In this section, we examine the spin–spin-correlation functions. Both the short-range and long-range behavior give detailed information on the phases and phase boundaries. Since there is no long-range magnetism (except in the ferromagnetic phase, where the order parameter commutes with the Hamiltonian), the correlation function is simply

$$O_s(i,j) = \langle \mathbf{S}_i \cdot \mathbf{S}_j \rangle, \tag{6}$$

where i and j are the indices specifying spin vertices in the lattice, Fig. 1.

A. Short-range correlations

To identify the bulk properties of the ground state, we plot six reference correlation functions in Fig. 7. There are the short-range correlations calculated for the central few sites of the 30×3 cylinder. The edges of the lattice show non-negligible boundary effects, however away from the boundary the bulk correlations appear to be representative of the thermodynamic limit and agree closely with correlators calculated using iDMRG. In Fig. 7, brown stripes indicate the phase transitions that we have identified.

B. Long-range correlations

We now consider the long-range behavior of the spin-spin correlators Eq. (6). One can choose different paths to study distant correlators according to the lattice geometry, but at long distances the spin-spin correlators are independent of the choice of path. Figure 8 shows correlators calculated for the path ACA as shown in the inset. We also calculated the correlation functions for a number of different paths. Up to trivial differences caused by the order in which different sublattices are listed, the results are insensitive to the path

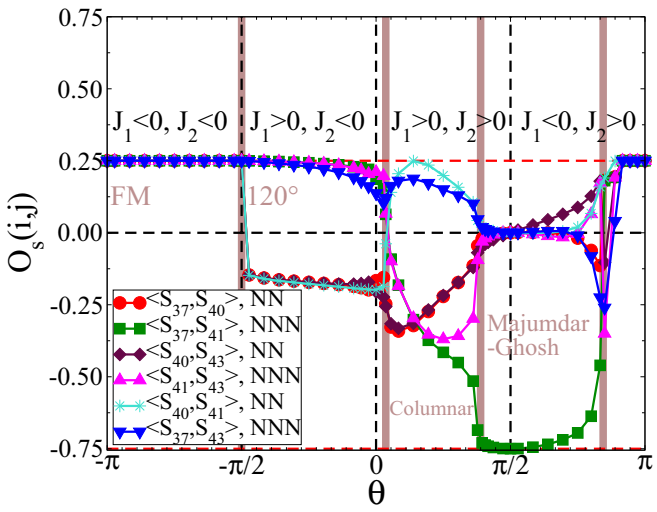

FIG. 7. (Color online) Short-ranged spin-spin correlation functions for the ground state on a 30×3 cylinder. S_n represents the spin operator for the site n according to the lattice numbering in Fig. 1. Dashed red lines are the limits of the correlation functions for spin-$\frac{1}{2}$ particles, $-3/4 \leqslant O_s(i,j) \leqslant 1/4$. Brown stripes indicate phase transitions.

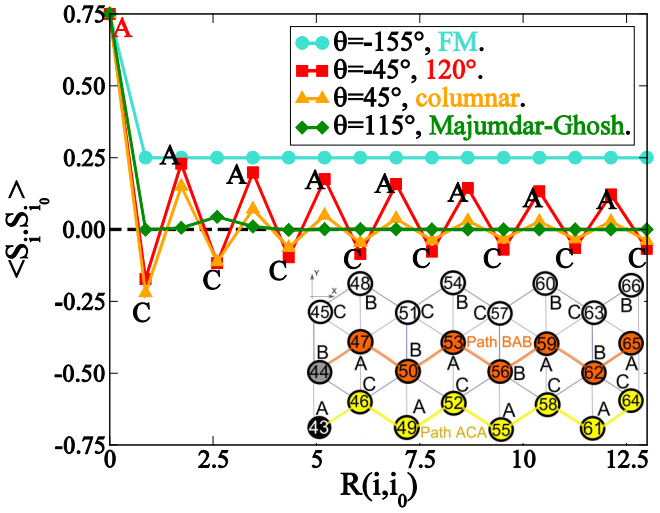

FIG. 8. (Color online) Spin-spin correlators for the THM on a 30×3 cylinder for trial path ACA. $R(i,i_0)$ is spatial distance between vertices i and i_0 in units of the lattice spacing. Two possible paths are shown in the inset.

followed. The results suggest that the 120° and columnar states are quasi-long-range and the Majumdar-Ghosh state contains only short-ranged spin-spin correlations.

Using iDMRG, one can directly extract the correlation length from the spectrum of the transfer matrix. If Λ is the largest magnitude eigenvalue in the transfer matrix smaller than 1, then the correlation length η is obtained from

$$|\Lambda| = e^{a_0/\eta}, \tag{7}$$

where a_0 is the size of the iDMRG unit cell. Upon increasing the number of states, m, the observation of power-law growth of the correlation length indicates a gapless phase, whereas

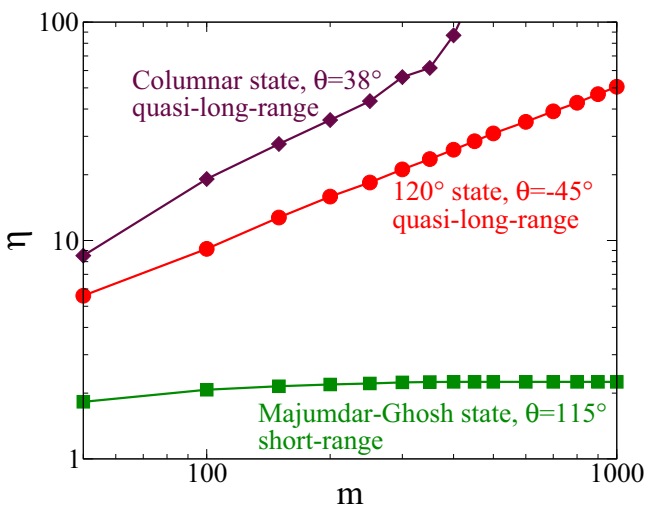

FIG. 9. (Color online) iDMRG results for the correlation length. η is the correlation length, calculated from the next-leading eigenvalue of the transfer matrix, Eq. (7). Power-law growth $\eta \propto m^{\kappa}$ indicates gapless quantum critical excitations with power-law correlations, while the saturation of the correlation length in the Majumdar-Ghosh region indicates that this phase is short range and gapped.

saturation of η is a sign of a gapped phase [56,57]. The results for the correlation length of the 120°, columnar, and Majumdar-Ghosh phases are shown in Fig. 9. This is consistent with finite DMRG results of Fig. 8, where the 120° and columnar states are quasi-long-range and the Majumdar-Ghosh phase has a finite correlation length.

V. CHIRALITY

For several decades, there has been much discussion [18,26,27,29,58] on the possibility of chiral order in the 2D model. A proper chiral order parameter will detect breaking of P and T symmetry of the wave function while the system preserves PT symmetry. This can be done by looking at order parameters or correlation functions that are not symmetric under P or T.

We studied the chirality using two chiral order parameters introduced below, Eqs. (11) and (14), which we evaluated using finite DMRG. The results are presented in Figs. 10 and 11. These results show that there is *no* long-range chiral order. We also directly measured the parity and time-reversal symmetry of infinite length three-leg cylinders, using infinite DMRG. The procedure for this is to calculate the overlap per unit cell of the iDMRG wave function with its conjugate or parity-reflected version. Since iDMRG works directly in the thermodynamic limit, spontaneous breaking of discrete symmetries can occur, and this is a reliable way to detect P or T symmetry breaking [7,47,59]. The calculated overlap, f, between the P-transformed, and T-transformed, wave functions is of the order of $1 - f \approx 10^{-8}$ per unit cell, showing that neither P nor T symmetry is broken.

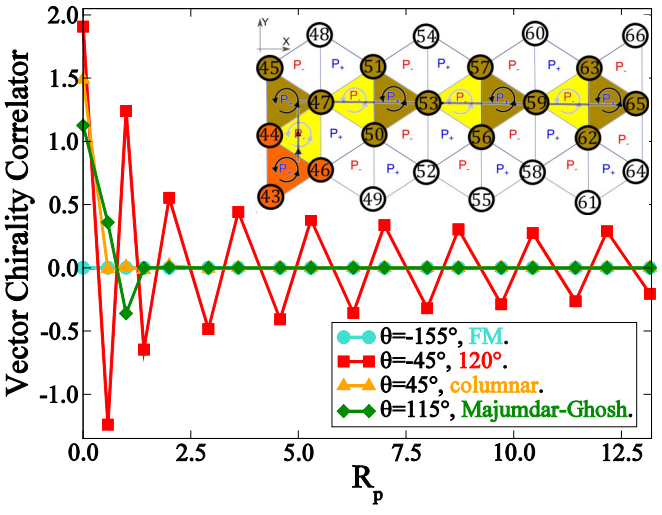

FIG. 10. (Color online) Vector chirality correlator, O_c, Eq. (11), on a 30×3 cylinder. R_P is the distance between the centers of the plaquettes in units of the lattice spacing. The antiferrochiral pattern in the 120° state can be explained by the tripartite symmetry of the lattice. Antiferrochirality is clearly broken in the Majumdar-Ghosh state. Inset: The path for which the vector chirality correlators were calculated. The P_+/P_- labels indicate the antiferrochiral ordering.

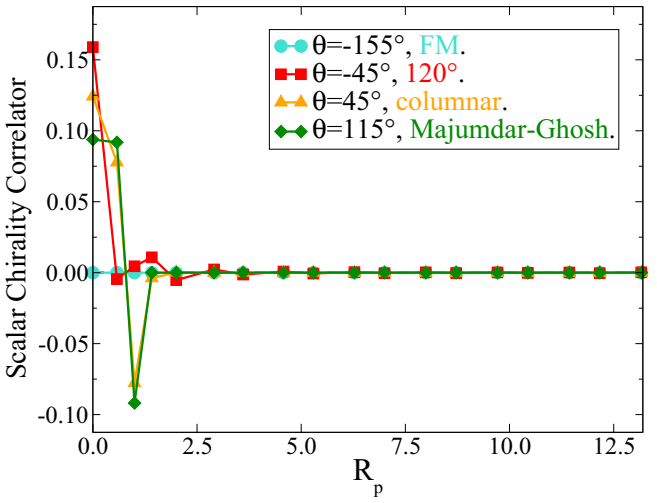

FIG. 11. (Color online) Scalar chirality correlator, O_t, Eq. (14), on a 30×3 cylinder. R_P is the distance between the center of plaquettes in units of the lattice spacing. The path chosen to calculate these correlators is the same as the inset of Fig. 10. The rapid reduction of O_t to zero at long range indicates that the phases are nonchiral and planar.

A. Vector chirality

To measure the local chirality, we use the cross product between vertex pairs in a plaquette, while keeping a fixed cyclic order of operators:

$$\mathbf{C}_c[A,B,C] = \mathbf{S}_A \times \mathbf{S}_B + \mathbf{S}_B \times \mathbf{S}_C + \mathbf{S}_C \times \mathbf{S}_A, \quad (8)$$

where $[A,B,C]$ stands for a triangular plaquette composed of vertices from sublattice A, B, and C. Note, however, that the magnitude of the local chirality is *not* a good order parameter, since it is easy to show that for any spin-$\frac{1}{2}$ system we have

$$(\mathbf{S}_i \times \mathbf{S}_j + \mathbf{S}_j \times \mathbf{S}_k + \mathbf{S}_k \times \mathbf{S}_i)^2 = -\tfrac{3}{4} M^2_{i,j,k} + \tfrac{45}{16}, \quad (9)$$

where $M^2_{i,j,k}$ is the square of the local magnetization:

$$M^2_{i,j,k} = (\mathbf{S}_i + \mathbf{S}_j + \mathbf{S}_k)^2. \quad (10)$$

Hence the magnitude of the cross product is directly related to the local magnetization and has no connection to the chirality.

The correlation function of the vector chirality, O_c, detects long-range chiral order:

$$O_c(i,j,k;i',j',k') = \langle \mathbf{C}_c[i,j,k] \cdot \mathbf{C}_c[i',j',k'] \rangle. \quad (11)$$

DMRG results for this correlation function are shown in Fig. 10. To calculate these correlators between desired plaquettes, we chose a path that has the maximum number of crossings of plaquette vertices. This path is shown in the inset of Fig. 10. The origin plaquette is indicated in red. The next two plaquettes, respectively, have two and one common vertices with the origin while longer-range plaquettes have none. The results of Fig. 10 suggest that the 120° and NNN Majumdar-Ghosh states are only short-range chiral. There is a quasi-long-range antiferrochiral pattern in the 120° state specified with P_+/P_- notation in the inset of Fig. 10, which is consistent with the tripartite structure of the lattice. We

calculated the vector chirality for all possible plaquettes, and all show the antiferrochirality of the 120° state.

B. Scalar chirality

A commonly considered chiral order parameter for the THM is the triple product on a triangular plaquette, known as the scalar chirality:

$$C_t[A,B,C] = \mathbf{S}_A.(\mathbf{S}_B \times \mathbf{S}_C). \quad (12)$$

The triple product operator breaks both P and T symmetries, and would acquire different signs for different plaquettes according to their chirality. A nonzero value of $C_t[A,B,C]$ also implies that the spins are nonplanar on that plaquette. As a result a nonchiral and planar system should acquire values close to zero for this triple product. Some studies [54,58] predict that the THM should be chiral in some circumstances (e.g., considering couplings higher than two-body exchange interactions), while the others [18,26,27,29] strongly suggest that the quantum fluctuations always select a planar spin arrangement, so there is no chiral symmetry breaking.

It is important to note that the square of the triple product, Eq. (12), on a single triangular plaquette is *not* a good order parameter to measure chirality, because it can be shown [60], similarly to the cross product, that for any spin-$\frac{1}{2}$ system

$$[\mathbf{S}_i \cdot (\mathbf{S}_j \times \mathbf{S}_k)]^2 = -\tfrac{1}{16} M^2_{i,j,k} + \tfrac{15}{64}. \quad (13)$$

As a result $\langle C_t^2[A,B,C]\rangle$ on a plaquette is directly related to the local magnetization and so is always nonzero, and gives no indication of the chirality.

A diagnostic for the chirality is the correlator of the scalar chirality:

$$O_t(i,j,k;i',j',k') = \langle C_t[i,j,k] C_t[i',j',k']\rangle. \quad (14)$$

The results for the scalar chirality correlator are presented in Fig. 11. The path here is same as the inset of Fig. 10. All phases other than FM show some short-range chiral correlations. However, the rapid drop of O_t to zero at long distance is a clear sign that all phases are nonchiral and planar.

VI. 120° ORDER PARAMETER

In the classical 120° state on the triangular lattice every NNN bond is aligned ferromagnetically, while NN sites form AFM bonds with uniform expectation values, $\langle \mathbf{S}_i.\mathbf{S}_j\rangle = -1/8$. This state appears in a semiclassical analysis [18].

The quantum analog of this classical 120° state can be constructed by positioning three spins at 120° angles on the Bloch sphere, forming a product state with long-range order at wave vector $\mathbf{Q} = (4\pi/\sqrt{3}, 4\pi/3)$, where the factor 2 arises from the rotation properties of spin-$\frac{1}{2}$ systems. The spin correlations are $\langle \mathbf{S}_i \cdot \mathbf{S}_j\rangle = S_i S_j \cos 120° = -1/8$ for each pair, which coincides with the classical value, as does the triple product $\mathbf{S}_A \cdot (\mathbf{S}_B \times \mathbf{S}_C) = 0$. The plaquette magnetization $(\mathbf{S}_A + \mathbf{S}_B + \mathbf{S}_C)^2 = 3/2$ is inherently nonclassical.

A suitable order parameter to detect this state is the squared sublattice magnetization of 120° state and can be constructed as

$$E^{120°} = \frac{1}{N_o} \sum_i \sum_{i'} \mathbf{S}_i \cdot \mathbf{S}_{i'} \times \cos\left[\frac{4\pi}{\sqrt{3}}(x_i - x_{i'})\right] \cos\left[\frac{4\pi}{3}(y_i - y_{i'})\right], \quad (15)$$

where $N_o = N(N+4)/8$ is a normalization factor. $E^{120°}$ will detect any state close to conventional 120° order. DMRG results for the squared sublattice magnetization of the 120° state on a 30×3 cylinder, $O^{120°} = \langle E^{120°}\rangle$, are shown in Fig. 12. The region with nonzero values of $O^{120°}$ in Fig. 12 is consistent with the 120° phase region of Fig. 3, showing that this is a good order parameter for the 120° phase. The value of sublattice magnetization for the NN model, $\sqrt{O^{120°}(\theta = 0)} \sim 49\%$ of the classical value, is comparable to previous calculations on the 2D model, 50% by ED [19], and 40% by CCM [30].

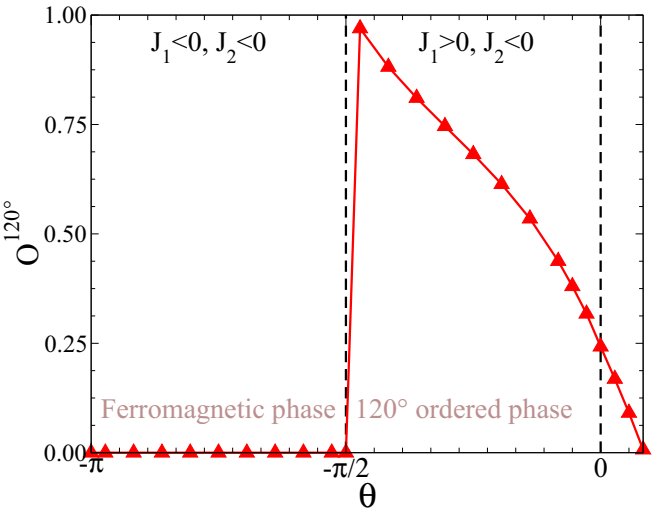

FIG. 12. (Color online) Squared sublattice magnetization of the 120° state on a 30×3 cylinder, $O^{120°}$. This order parameter correctly identifies the 120° phase, consistent with the spin-spin correlations, Fig. 7.

The 120° order parameter is close to maximal in the limit $\theta \to -\pi/2$, where the ground state tends toward the quantum counterpart of the classical 120° state. This limit can be understood as fully saturated ferromagnetism on each sublattice due to the large negative J_2; a small positive J_1 then induces 120° ordering between the sublattices.

VII. PHASE TRANSITIONS AND CRITICAL POINTS

In this section we pinpoint the location of the phase transitions and their nature, determined from the magnetization, order parameters, and spin gaps.

The point $\theta = -\pi/2$ marks rapid changes in many observables, consistent with a first-order transition. Indeed, since $J_1 = 0$ at this point, the ground state consists of three uncoupled sublattices, with ferromagnetic bonds within each sublattice, as discussed in Sec. III. Therefore the ground state

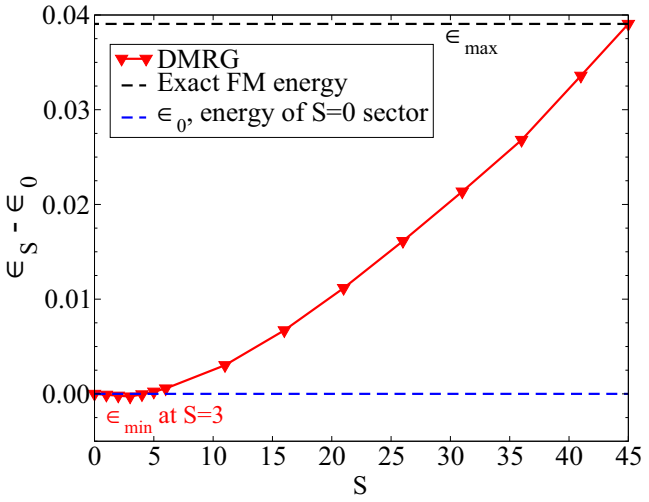

FIG. 13. (Color online) Difference between energy per bond of partially polarized states and the nonpolarized state on a 30×3 cylinder at $\theta = 153^\circ$, near the critical point $\theta_c = 152.0^\circ$. S is the total spin, which is a good quantum number. The curve has its minimum at a nonzero polarization, which indicates that there is a second-order phase transition close to this point.

is $N/2$-fold degenerate, and hence the 120° state and the fully polarized ferromagnet coexist.

To study the nature of the phase transition at $\theta_c = 152.0^\circ$ (NNN Majumdar-Ghosh to ferromagnet), we calculated the lowest-energy state in every possible total spin sector. At points near the transition, we found a partially polarized ground state. For example, at $\theta = 153^\circ$, shown in Fig. 13, the ground state for a 30×3 cylinder has total spin $S = 3$. This indicates a *second-order* transition. We also calculated the ground-state magnetization around the critical point, which is shown in Fig. 14. The obtained transition point indicated by the brown stripe is consistent with the correlation function results from Fig. 7.

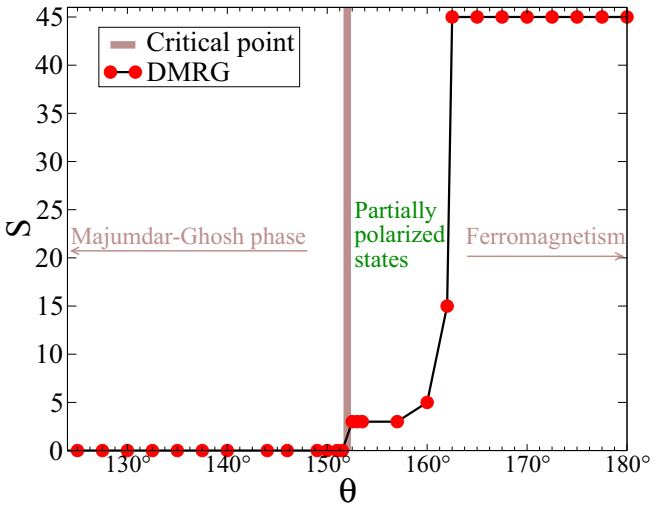

FIG. 14. (Color online) Magnetization (ground-state spin polarization) around the critical point $\theta_c = 152.0^\circ$ on a 30×3 cylinder. The onset of the phase transition is indicated with the brown stripe.

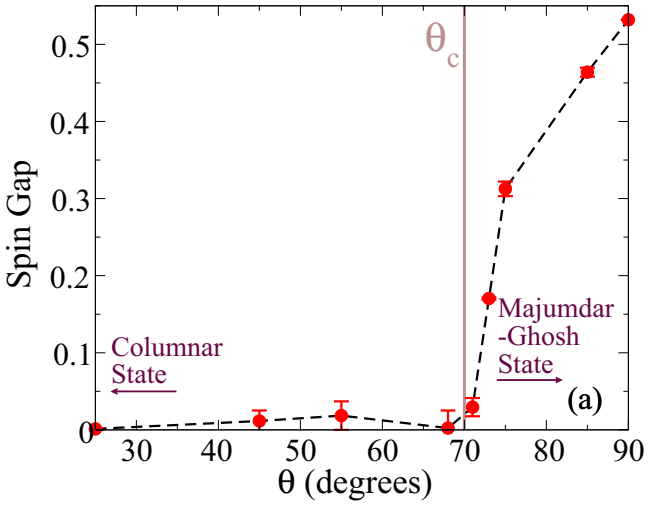

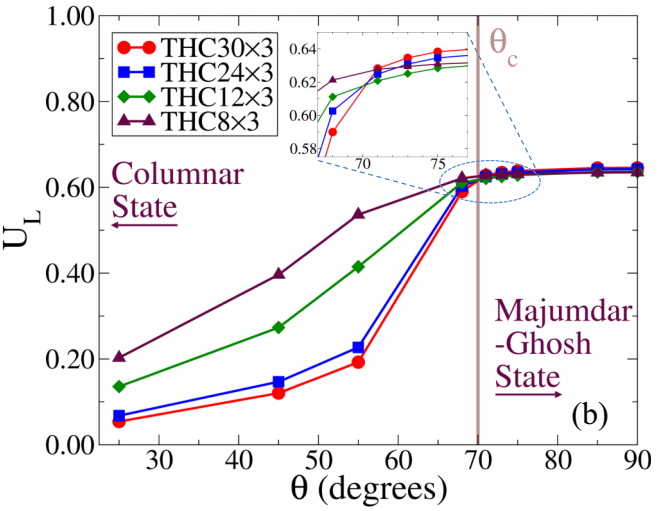

FIG. 15. (Color online) (a) Spin gap extrapolated to the thermodynamic limit. (b) Binder cumulant of the dimer order parameter, Eq. (16), for the columnar to Majumdar-Ghosh phase transition.

The elementary excitations in the Majumdar-Ghosh chain are pairs of spin-$\frac{1}{2}$ solitons [61]. In the NNN Majumdar-Ghosh phase of the three-leg ladder, our numerical calculations show that the solitons in each sublattice are pinned to each other, forming a dislocation line. Hence the elementary excitations are pairs of dislocations, with total spin $S = 3$.

Accurately locating the phase transition from the Majumdar-Ghosh state into the gapless columnar state is more difficult. Deep in the columnar phase, finite-size scaling of the spin gap is consistent with zero gap, as expected. But the finite-size scaling is difficult to perform near the phase boundary because the finite-size corrections in the two phases scale differently. Hence the spin gap has fairly large error bars in this region, and the exact transition is difficult to identify. One can use instead the dimer order parameter, defined for this model as

$$D_{(A)} = \frac{3}{N} \sum_{\langle\langle i,j\rangle\rangle \in A} (-1)^i \mathbf{S}_i \cdot \mathbf{S}_j, \qquad (16)$$

where the sum is over all NNN spins in one sublattice. However, the dimer order parameter also contains large finite-size corrections. A standard procedure (although not common in DMRG calculations) is to use higher moments of the order parameter to cancel out low-order finite-size effects, for example, using the Binder cumulant [62]:

$$U_L = 1 - \frac{\langle D^4 \rangle}{3\langle D^2 \rangle^2}. \tag{17}$$

The spin gap and Binder cumulant of the dimer order parameter are shown in Fig. 15. To obtain the spin gap, we first calculated the gap between $S = 0$ and 1 total spin sectors for finite-length cylinders. The gap was extrapolated to the thermodynamic limit, Fig. 15(a), using the $L^{-3/2}$ scaling identified by Neuberger and Ziman [63], which produces a good fit except very close to the transition to the gapped Majumdar-Ghosh phase. The Binder cumulant, Fig. 15(b), shows the expected behavior, whereby the value of the Binder cumulant at the phase transition is independent of the lattice size (up to higher-order corrections). The curves for 12×3, 24×3, and 30×3 intersect quite closely, indicating that the transition is in the vicinity of $\theta = 70.0^\circ$.

The columnar and 120° phases are both gapless, but we identify the location of the phase transition from the vanishing of the short-range O^{120° order parameter shown in Fig. 12, giving the transition point as $\theta \simeq 6.5^\circ$.

VIII. CONCLUSION

We have performed a comprehensive study of the phase diagram of the triangular J_1-J_2 model on a three-leg cylinder, using both finite DMRG and iDMRG methods. There are four distinct phases in this model. All phases are nonchiral and planar. The 120° and columnar phases are gapless with quasi-long-range correlations. For large $J_2 > 0$, the geometry of the ladder results in a Majumdar-Ghosh-like phase with long-range dimer order and a twofold degenerate ground state. This phase is an effect of the restricted geometry, and only exists for $L \times 3$ and $L \times 4$ cylinders.

Because we use a finite-width chain, the absence of SU(2) symmetry-breaking magnetic ordering means that the long-range physics is rather different to the 2D model. In the true 2D model, both the 120° and columnar phases are expected to be SU(2)-broken long-range ordered. Thus, on increasing the width of the cylinder, we expect that the correlations will increase in magnitude and the gapless modes arising from the 1D criticality will evolve into Goldstone modes associated with the broken symmetry of the order parameter.

The short-range physics and structure of the phase diagram of the three-leg ladder agrees closely with known results for the 2D model, especially in the small J_2 region. We find a transition from 120° to columnar phases at $\theta_c \simeq 6.5^\circ$, close to the classical value. Further studies on larger width cylinders have clarified that between the 120° and columnar state there is a spin liquid region [64], consistent with the recent results of quantum Monte Carlo calculations [31,32].

The boundary between 1D and 2D physics in this model is rather rich, and this suggests that the physics arising from restricting geometry to finite-width ladders presents a fruitful direction for future investigation, and may explain some novel properties of molecular solids [65].

ACKNOWLEDGMENTS

We thank C. Janani and F. Zhan for useful discussions. This work has been supported by the Australian Research Council Centre of Excellence for Engineered Quantum Systems, Grant No. CE110001013. B.J.P. is supported by the Australian Research Council under Grant No. FT130100161. After completion of this work, we became aware of some related results [66,67].

[1] S. Sachdev, *Quantum Phase Transitions*, 2nd ed. (Cambridge University, Cambridge, 2011), Chap. 19.
[2] C. Lhuilier and G. Misguich, *Frustrated Quantum Magnets in High Magnetic Fields*, Lecture Notes in Physics Vol. 595 (Springer-Verlag, Berlin, 2001), p. 161.
[3] A. Auerbach, *Interacting Electrons and Quantum Magnetism* (Springer-Verlag, New York, 1994).
[4] A. M. Tsvelik, *Quantum Field Theory in Condensed Matter Physics* (Cambridge University, Cambridge, 2003).
[5] C. K. Majumdar and D. Ghosh, J. Math. Phys. **10**, 1388 (1969).
[6] I. Affleck, T. Kennedy, E. H. Lieb, and H. Tasaki, Phys. Rev. Lett. **59**, 799 (1987).
[7] F. Pollmann, E. Berg, A. M. Turner, and M. Oshikawa, Phys. Rev. B **85**, 075125 (2012).
[8] L. Balents, Nature (London) **464**, 199 (2010).
[9] B. J. Powell and R. H. McKenzie, Rep. Prog. Phys. **74**, 056501 (2011).
[10] X. Chen, Z.-C. Gu, and X.-G. Wen, Phys. Rev. B **82**, 155138 (2010).
[11] X.-L. Qi and S.-C. Zhang, Rev. Mod. Phys. **83**, 1057 (2011).
[12] *High-Temperature Superconductors*, edited by W. G. Qiu, Woodhead Publishing Series in Electronic and Optical Materials, 1st ed. (Elsevier, Cambridge, 2011).
[13] T. Pang, *An Introduction to Computational Physics*, 2nd ed. (Cambridge University, Cambridge, 2011).
[14] E. Dagotto, Rep. Prog. Phys. **62**, 1525 (1999).
[15] E. H. Kim, Ö. Legeza, and J. Sólyom, Phys. Rev. B **77**, 205121 (2008).
[16] P. W. Anderson, Mater. Res. Bull. **8**, 153 (1973).
[17] Th. Jolicoeur and J. C. Le Guillou, Phys. Rev. B **40**, 2727(R) (1989).
[18] Th. Jolicoeur, E. Dagotto, E. Gagliano, and S. Bacci, Phys. Rev. B **42**, 4800(R) (1990).
[19] B. Bernu, P. Lecheminant, C. Lhuillier, and L. Pierre, Phys. Rev. B **50**, 10048 (1994).
[20] C. Janani, J. Merino, I. P. McCulloch, and B. J. Powell, Phys. Rev. Lett. **113**, 267204 (2014); Phys. Rev. B **90**, 035120 (2014).
[21] A. C. Jacko, C. Janani, K. Koepernik, and B. J. Powell, Phys. Rev. B **91**, 125140 (2015).

[22] L. E. Svistov, A. I. Smirnov, L. A. Prozorova, O. A. Petrenko, L. N. Demianets, and A. Y. Shapiro, Phys. Rev. B **67**, 094434 (2003).

[23] S. A. Zvyagin, D. Kamenskyi, M. Ozerov, J. Wosnitza, M. Ikeda, T. Fujita, M. Hagiwara, A. I. Smirnov, T. A. Soldatov, A. Ya. Shapiro, J. Krzystek, R. Hu, H. Ryu, C. Petrovic, and M. E. Zhitomirsky, Phys. Rev. Lett. **112**, 077206 (2014).

[24] O. A. Starykh, W. Jin, and A. V. Chubukov, Phys. Rev. Lett. **113**, 087204 (2014).

[25] R. Coldea, D. A. Tennant, A. M. Tsvelik, and Z. Tylczynski, Phys. Rev. Lett. **86**, 1335 (2001).

[26] E. Dagotto and A. Moreo, Phys. Rev. Lett. **63**, 2148 (1989).

[27] R. Deutscher and H. U. Everts, Z. Phys. B Con. Mat. **93**, 77 (1993).

[28] J. E. Hirsch and S. Tang, Phys. Rev. B **39**, 2887(R) (1989).

[29] A. V. Chubukov and Th. Jolicoeur, Phys. Rev. B **46**, 11137 (1992).

[30] P. H. Y. Li, R. F. Bishop, and C. E. Campbell, Phys. Rev. B **91**, 014426 (2015).

[31] R. V. Mishmash, J. R. Garrison, S. Bieri, and C. Xu, Phys. Rev. Lett. **111**, 157203 (2013).

[32] R. Kaneko, S. Morita, and M. Imada, J. Phys. Soc. Jpn. **83**, 093707 (2014).

[33] L. Messio, C. Lhuillier, and G. Misguich, Phys. Rev. B **83**, 184401 (2011).

[34] L. Capriotti, A. E. Trumper, and S. Sorella, Phys. Rev. Lett. **82**, 3899 (1999).

[35] E. Y. Loh, Jr., J. E. Gubernatis, R. T. Scalettar, S. R. White, D. J. Scalapino, and R. L. Sugar, Phys. Rev. B **41**, 9301 (1990).

[36] R. Orus, Ann. Phys. **349**, 117 (2014).

[37] F. Verstraete and J. I. Cirac, arXiv:cond-mat/0407066.

[38] L. Seabra, T. Momoi, P. Sindzingre, and N. Shannon, Phys. Rev. B **84**, 214418 (2011).

[39] F. Mezzacapo and J. I. Cirac, New J. Phys. **12**, 103039 (2010).

[40] K. Harada, Phys. Rev. B **86**, 184421 (2012).

[41] U. Schollwöck, Ann. Phys. (NY) **326**, 96 (2011).

[42] S. R. White, Phys. Rev. Lett. **69**, 2863 (1992).

[43] I. P. McCulloch, J. Stat. Mech. (2007) P10014.

[44] E. M. Stoudenmire and S. R. White, Annu. Rev. Condens. Matter Phys. **3**, 111 (2012).

[45] F. Kolley, S. Depenbrock, I. P. McCulloch, U. Schollwöck, and V. Alba, Phys. Rev. B **91**, 104418 (2015).

[46] R. Chen, H. Ju, H.-C. Jiang, O. A. Starykh, and L. Balents, Phys. Rev. B **87**, 165123 (2013).

[47] I. P. McCulloch, arXiv:0804.2509v1.

[48] J. W. G. Wildöer, L. C. Venema, A. G. Rinzler, R. E. Smalley, and C. Dekker, Nature (London) **391**, 59 (1998).

[49] N. D. Mermin and H. Wagner, Phys. Rev. Lett. **17**, 1133 (1966).

[50] M. Getzlaff, *Fundamentals of Magnetism* (Springer, Berlin, 2007), Chap. 5.

[51] P. Lecheminant, B. Bernu, C. Lhuillier, and L. Pierre, Phys. Rev. B **52**, 6647 (1995).

[52] C. J. Gazza and H. A. Ceccatto, J. Phys.: Condens. Matter **5**, L135 (1993).

[53] Z. Weihong, R. H. McKenzie, and R. R. P. Singh, Phys. Rev. B **59**, 14367 (1999).

[54] H. Nishimori and H. Nakanishi, J. Phys. Soc. Jpn. **57**, 626 (1988).

[55] H. Nishimori and S. J. Miyake, Prog. Theor. Phys. **73**, 18 (1985).

[56] L. Tagliacozzo, T. R. de Oliveira, S. Iblisdir, and J. I. Latorre, Phys. Rev. B **78**, 024410 (2008).

[57] V. Stojevic, J. Haegeman, I. P. McCulloch, L. Tagliacozzo, and F. Verstraete, Phys. Rev. B **91**, 035120 (2015).

[58] G. Baskaran, Phys. Rev. Lett. **63**, 2524 (1989); S. E. Korshunov, Phys. Rev. B **47**, 6165 (1993).

[59] F. Heidrich-Meisner, I. P. McCulloch, and A. K. Kolezhuk, Phys. Rev. B **80**, 144417 (2009).

[60] X. G. Wen, F. Wilczek, and A. Zee, Phys. Rev. B **39**, 11413 (1989).

[61] B. S. Shastry and B. Sutherland, Phys. Rev. Lett. **47**, 964 (1981).

[62] K. Binder, Z. Phys. B **43**, 119 (1981).

[63] H. Neuberger and T. Ziman, Phys. Rev. B **39**, 2608 (1989).

[64] S. N. Saadatmand and I. P. McCulloch (unpublished).

[65] J. Fraxedas, *Molecular Organic Materials: From Molecules to Crystalline Solids* (Cambridge University, Cambridge, 2006).

[66] Z. Zhu and S. R. White, arXiv:1502.04831v1.

[67] W.-J. Hu, S.-S. Gong, W. Zhu, and D. N. Sheng, arXiv:1504.00654v1.